Volume 14
Number 48
28 December 2022
Pages 17807-18256

Nanoscale

rsc.li/nanoscale

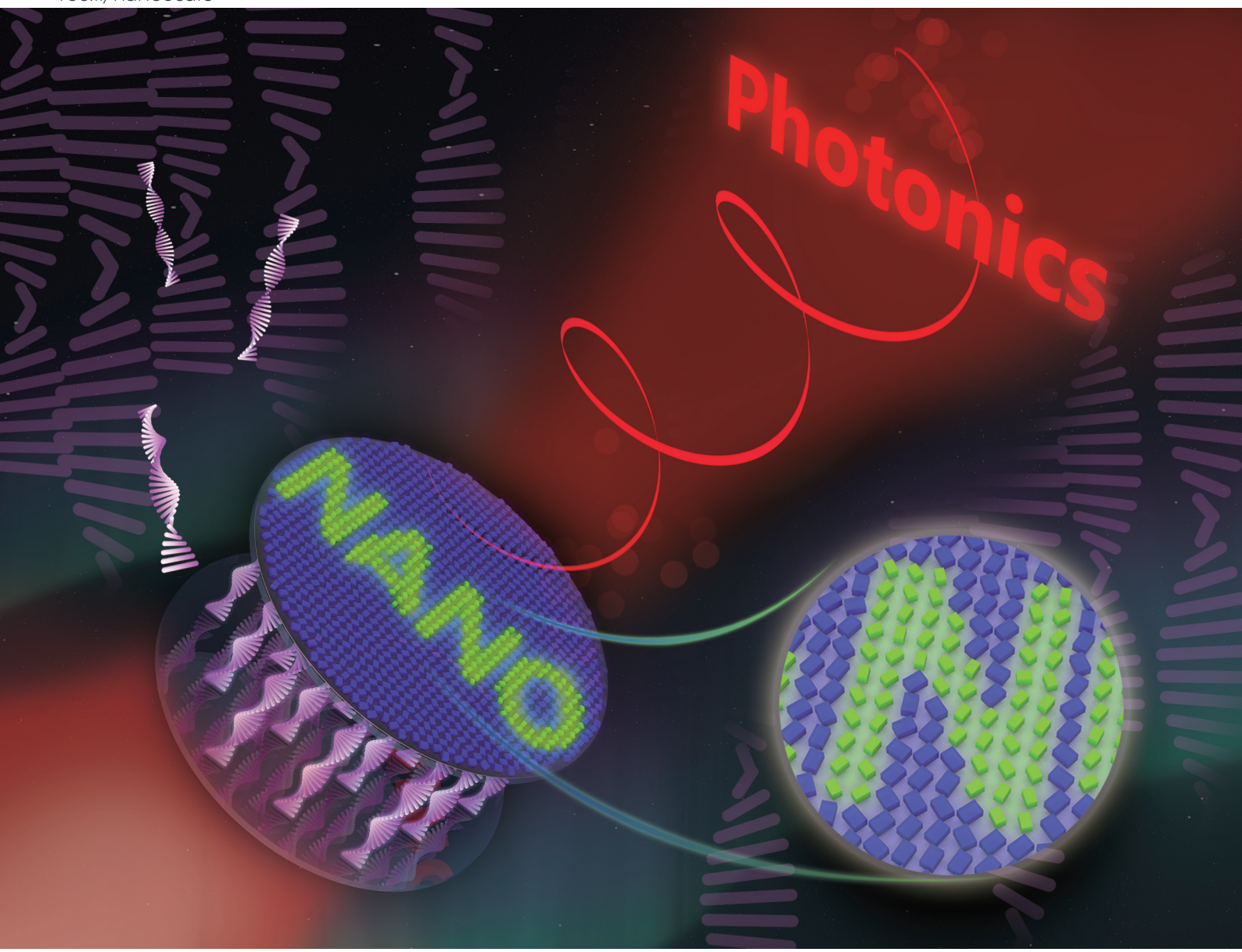

ISSN 2040-3372

ROYAL SOCIETY OF CHEMISTRY

PAPER
Yan-Qing Lu, Yan Jun Liu *et al.*
Cholesteric liquid crystal-enabled electrically programmable metasurfaces for simultaneous near- and far-field displays

NCNST

Nanoscale

PAPER

View Article Online
View Journal | View Issue

Cite this: *Nanoscale*, 2022, **14**, 17921

Cholesteric liquid crystal-enabled electrically programmable metasurfaces for simultaneous near- and far-field displays†

Jiawei Wang, [a] Wenfeng Cai,[a] Huilin He,[a] Mengjia Cen,[a] Jianxun Liu, [a] Delai Kong,[a] Dan Luo, [a] Yan-Qing Lu*[b] and Yan Jun Liu *[a]

Received 29th September 2022,
Accepted 14th November 2022

DOI: 10.1039/d2nr05374h

rsc.li/nanoscale

Metasurfaces can enable polarization multiplexing of light so as to carry more information. Specific polarized light necessitates bulk polarizers and waveplates, which significantly increases the form size of metasurface devices. We propose an electrically programmable metasurface enabled by dual-frequency cholesteric liquid crystals (DF-CLCs) for simultaneous near- and far-field displays. Moreover, the integrated device can be electrically programmed to demonstrate 6 different optical images by engineering the DF-CLCs with frequency-modulated voltage pulses. Such programmable metasurfaces are potentially useful for many applications including information storage, displays, anti-counterfeiting, and so on.

1. Introduction

Metasurfaces are artificially designed two-dimensional (2D) planar surfaces that consist of subwavelength meta-atoms. By changing the size or orientation of meta-atoms, metasurfaces are able to modify electromagnetic fields arbitrarily including the phase,[1–4] polarization,[4–7] amplitude,[8–10] frequency,[10–13] and so forth. Featuring ultrathin thickness and subwavelength-scale unit, metasurfaces possess the advantages of low loss, high resolution, high compatibility, and easy integration, boosting the development of integrated electromagnetic devices.[14,15] Thereinto, metasurface holograms have attracted significant attention due to their great potential in display, security, and data storage applications.[16–19] Recently, some efforts have been made to encode information to multiple channels within a single metasurface to achieve integration and multiple functions.[20,21] However, the degree of freedom in a single metasurface is limited, moreover, the change of the geometric parameters and orientation of the meta-atoms may cause undesirable optical responses. A new approach to further increase the degree of freedom is to exploit two or more meta-atoms arranged as a supercell to form staggered or stacked metasurfaces in space.[22–25] However, due to the superposition of different meta-atoms, it may cause undesirable couplings and interferences between the meta-atoms. In addition, the difficulties of designing and manufacturing are particularly prominent. In order to expand the information capacity, recently, a design method of single meta-atoms for dual channels has been proposed to achieve nano-printing and holographic displays simultaneously.[26,27] Thus far, all the above-mentioned metasurfaces exploit polarization multiplexing to activate different information channels. The polarization multiplexing requires a bulk polarizer and waveplate to generate the desired polarization for information decoding in the metasurface. As a result, the whole system loses the advantages of compactness and lightness.

To eliminate bulky optical components, it is highly desirable to develop compact, on-chip, and multifunctional polarization controllers for the designed metasurfaces. Meanwhile, active metasurfaces have also emerged as an intensively explored field in recent years.[28–42] Along this line, liquid crystals (LCs) could play a key role due to their unique properties. LCs possess large birefringence, broad spectral working range, excellent compatibility and versatile driving methods.[43–45] Due to their large birefringence, they have been widely used for phase and polarization modulation. Researchers have developed nematic LC modulators to replace polarizers and/or waveplates for polarization multiplexing in metasurfaces.[33–38] These studies provide a good scheme for the compact, dynamic and versatile modulation of the optical field. However, nematic LCs are incompetent for optical field modulation under unpolarized and arbitrary linearly polarized light sources. In contrast, cholesteric liquid crystals (CLCs) can overcome the polarization-dependence of the light source, regardless of being unpolarized or linearly polarized, and they can be

[a]*Department of Electrical and Electronic Engineering, Southern University of Science and Technology, Shenzhen, 518055, China. E-mail: yjliu@sustech.edu.cn*
[b]*College of Engineering and Applied Sciences, Nanjing University, Nanjing 210093, China. E-mail: yqlu@nju.edu.cn*

† Electronic supplementary information (ESI) available. See DOI: https://doi.org/10.1039/d2nr05374h

applied for the generation and modulation of circular polarization.[46–49] Therefore, a CLC cell could replace a linear polarizer (LP) and a quarter-waveplate (QWP) to produce circularly polarized light within its bandgap regime. Furthermore, the use of dual-frequency cholesteric liquid crystals (DF-CLCs) can add one more degree of electrically controlled states. The introduction of DF-CLCs provides new opportunities for active multifunctional metasurfaces. Thus far, CLC-based holograms and structural colors have been reported.[50–54] However, given the alignment techniques of CLCs, it is still quite challenging to achieve the high resolution of less than 1 μm. By integrating CLCs with metasurfaces, one could achieve high-resolution, dynamic holograms and structural colors simultaneously.

In this work, we propose an electrically programmable metasurface enabled by dual-frequency cholesteric liquid crystals (DF-CLCs) for simultaneous near- and far-field displays. A single metasurface can be designed to provide high-efficiency near-field structural colors and far-field hologram displays. DF-CLCs can be integrated with metasurfaces to fulfil the required incident polarizations, which can be programmable *via* applying an external electric field. By integrating DF-CLCs and designed metasurfaces, both near- and far-field displays can be simultaneously demonstrated. Our proposed system presents highly integrated, compact, and programmable features, and is potentially useful for holographic displays, anti-counterfeit coding, and other applications.

2. Results and discussion

2.1 Dielectric metasurfaces for both near- and far-field displays

The phase, amplitude, and polarization of light can be precisely controlled by carefully engineering the dimensions and constituting materials of meta-atoms. In particular, the desired phase can be achieved through two strategies: propagation and geometric phase engineering. This is accomplished by carefully designing the meta-atoms, which is often carried out by changing the long and short axes and the rotation angles of meta-atoms. For a uniaxial meta-atom acting as a phase plate, its Jones matrix can then be written as:

$$J = R(-\alpha)\begin{bmatrix} e^{i\varphi_x} & 0 \\ 0 & e^{i\varphi_y} \end{bmatrix} R(\alpha), \quad (1)$$

where φ_x and φ_y are the phase shifts for linearly polarized light along the fast and slow axes, respectively, rotated by an angle α relative to the reference coordinate system. $R(\alpha)$ is a 2 × 2 rotation matrix given by:

$$R(\alpha) = \begin{bmatrix} \cos\alpha & \sin\alpha \\ -\sin\alpha & \cos\alpha \end{bmatrix}. \quad (2)$$

The propagation phase can be generated by changing the long and short axes of the meta-atoms while keeping the angle α unaltered. The geometric phase, or called the Pancharatnam–Berry (PB) phase, is achieved with the meta-atoms acting as half-wave plates, *i.e.*, by ensuring $|\varphi_x - \varphi_y| = \pi$, and then rotating the meta-atoms to set the phase profile $\varphi(x, y) = 2\alpha(x, y)$ of the circular polarization states, where α is the rotation angle of the meta-atoms. Therefore, the PB phase can be controlled linearly from 0 to 2π by rotating the axis from 0 to π. If the meta-atoms convert an incident beam with left-handed circular polarization (LCP) to a transmitted beam with right-handed circular polarization (RCP), an additional PB phase will arise, and *vice versa*. In contrast, the transmitted beam with the same polarization as the incident one does not give rise to the PB phase modulation. This principle can be exploited to design a hologram at the desired wavelength in the *k*-space. The *k*-space hologram illustration is defined as the far-field display in this work. In contrast, the structural coloration-resulted image in real space is defined as the near-field display. Upon the incidence on the meta-atom with unpolarized light, the transmission in the visible range is given by:

$$T(\lambda) = [T_x(\lambda) + T_y(\lambda)]/2, \quad \lambda \in [400, 800], \quad (3)$$

where λ is the operating wavelength, $T_x(\lambda)$ and $T_y(\lambda)$ represent the transmittance of a meta-atom along the long (*x*-axis) and short (*y*-axis) axes, respectively. Therefore, upon unpolarized light incidence, a designed metasurface consisting of arranged meta-atoms with different geometric sizes can produce near-field displays in real-space *via* structural coloration and far-field displays in the *k*-space *via* diffraction upon circular polarized light incidence as well.

In our design, anisotropic nanorods are used to simultaneously engineer phase and spectral properties. Fig. 1(a) shows the structure of a single meta-atom, which is a silicon nitride nanorod on a glass substrate. Using the finite-difference time-domain (FDTD) method, a series of meta-atoms were simulated, and two meta-atoms were finally selected. Fig. 1(b) depicts the simulated cross-polarized (LCP and RCP) transmission of two meta-atoms. One meta-atom (defined as meta-atom-I) is 300 nm in length and 70 nm in width, and the

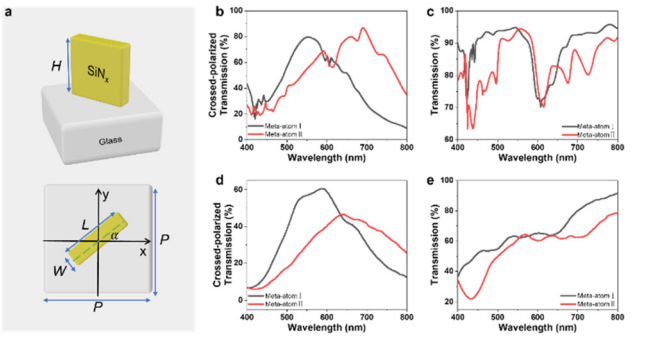

Fig. 1 (a) Schematic illustration of a single silicon nitride meta-atom on a glass substrate (3D- and top-views in the upper and lower rows) with the height of H = 900 nm and the period of P = 600 nm. The simulated (b and c) and measured (d and e) transmission spectra for the designed meta-atom-I (W = 70 nm and L = 300 nm) and meta-atom-II (W = 100 nm and L = 350 nm) under the LCP light incidence with a RCP analyzer (b and d) and unpolarized light incidence without any analyzer (c and e), respectively.

other one (defined as meta-atom-II) is 350 nm in length and 100 nm in width, both of which are 900 nm in height and 600 nm in period with square arrangement. From Fig. 1(b), it can be seen that both meta-atoms have approximately the same transmission of 60% at a wavelength of 633 nm, under the LCP light incidence. It is worth mentioning that the propagation phase ψ caused by the meta-atoms will also contribute to the total phase modulation. However, the calculated propagation phases for both designed meta-atoms are $\psi_{I,x}$ = 3.09, $\psi_{I,y}$ = 1.66, $\psi_{II,x}$ = 3.10, and $\psi_{II,y}$ = 1.70, which are approximately the same along the x- and y-axes, respectively. Therefore, the propagation phases can be neglected due to their same contribution. As a result, only the induced PB phases of two meta-atoms contribute to the total phase modulation at the wavelength of 633 nm. That is to say, the two designed meta-atoms with different geometric sizes are nearly perfect clones for phase modulation. Using these two meta-atoms, we can design a vectorial hologram using 8-level PB phase-based pixelated metasurfaces. Under the incidence of an unpolarized light beam, the simulated spectra of the two meta-atoms are shown in Fig. 1(c). In our simulation, we used the experimentally measured refractive index of silicon nitride (see Fig. S1†). We measured the cross-polarized and co-polarized transmission of these two meta-atom arrays under the LCP light incidence, as shown in Fig. 1(d) and Fig. S2,† respectively. The optical setup for the transmission measurement is schematically illustrated in Fig. S3.† At 633 nm, the two meta-atom arrays have the same cross-polarized transmittance of ~45%, which is less than the calculated one of 60%. The measured transmittance under the unpolarized light incidence is also shown in Fig. 1(e). There is a significant difference in the visible transmission spectrum between the two typical meta-atoms. Meta-atom-II has an apparent dip at ~430 nm, while meta-atom-I has no characteristic peaks or dips. As a result, they have different structural colors: meta-atom-I is light purple, while meta-atom-II is yellow-green. The measured transmittance in Fig. 1(e) is also less than the calculated one in Fig. 1(c). This difference in the measured and calculated transmittance could be mainly attributed to nanofabrication errors and the surface roughness of the meta-atoms. Overall, the measured cross-polarized transmittance spectra follow the roughly same profiles with the simulated ones.

Experimentally, we carried out the nanofabrication of the designed metasurface with electron beam lithography and dry etching. We then observed near-field structural color displays in real-space and far-field holographic images in the k-space. Fig. 2(a) shows the typical scanning electron microscopy (SEM) image of the fabricated metasurface with the designed pattern. The inset shows the magnified patterns consisting of two designed meta-atoms, in which meta-atom-I and meta-atom-II are used for the background and the letter coding. Fig. 2(b) illustrates a three-dimensional SEM view of the arranged meta-atoms with a tilted view angle of 75°. It can be clearly seen that the meta-atoms have smooth surfaces and vertical sidewalls, indicating high-quality nanofabrication. On the one hand, by putting the fabricated metasurface under an optical microscope with a halogen light source, we can clearly observe a colored image with the "NANO" letters, *i.e.*, the so-called near-field display in this work, which is produced through the designed structural coloration. The letters demonstrate an apparent yellow-green appearance with a uniform light purple background, as shown in Fig. 2(c). On the other hand, upon 633 nm laser beam incidence with circular polarization, the same fabricated metasurface works as a hologram, diffracting another image with the "photonics" letters, *i.e.*, the so-called far-field display in the k-space in this work, as shown in Fig. 2(d). The diffracted image shows high quality without any stray light. Therefore, only a single metasurface can simultaneously produce both near- and far-field displays, hence enhancing the information storage. We observed structurally colored images of cross-polarized (LCP to RCP) and co-polarized (LCP to LCP) transmittance, as shown in Fig. S4.†

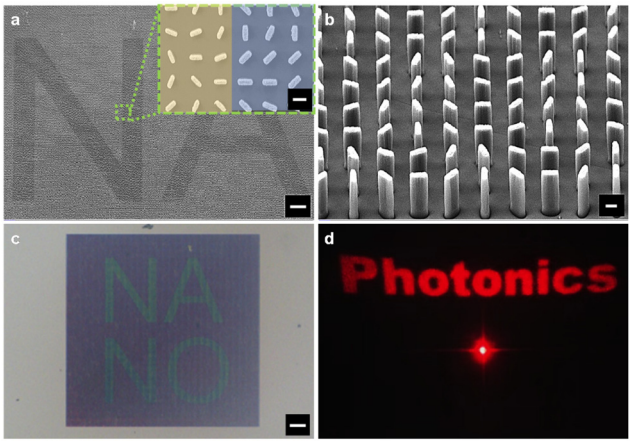

Fig. 2 (a) Typical SEM image of the fabricated metasurfaces. Scale bar: 20 μm. The inset is the magnified view of two types of meta-atoms. Scale bar: 300 nm. (b) A 75° view SEM image of the metasurface. Scale bar: 200 nm. (c) Structural coloration-induced displays of the bare metasurface under unpolarized light incidence. Scale bar: 50 μm. (d) Diffracted hologram of the bare metasurface under the circularly polarized 633 nm laser beam incidence.

2.2 DF-CLCs for polarization control

From the aforementioned discussion, it can be inferred that our proposed metasurface requires incident light with different polarizations to display near- and far-field information. Therefore, it is highly desirable to have an optical device to conveniently produce the on-demand light polarization, which can be efficiently integrated with the metasurface. Along this line, DF-CLCs could be an excellent candidate that can be well integrated with metasurfaces and generate various polarization states. DF-CLCs are able to exhibit three optically stable states: planar state, focal conic state, and homeotropic state, as shown in Fig. 3(a)–(c). These three states can be inter-transformed by applying frequency-modulated voltage pulses. In the planar state, DF-CLCs are able to change the incident unpolarized light into circularly polarized light since the LC molecules form a superhelical structure; in the focal conic

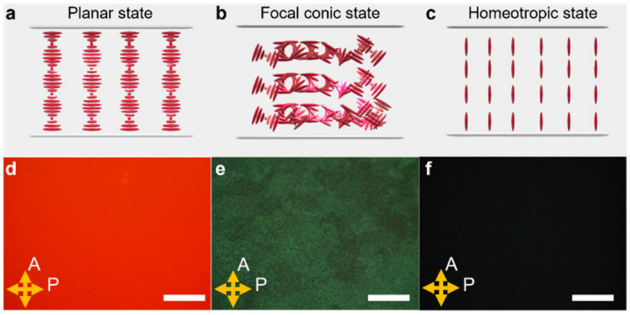

Fig. 3 (a–c) Schematic diagram of the DF-CLC operating principle in the planar state, the focal conic state, and the homeotropic state, respectively. (d–f) Typical POM images of the DF-CLC cell working in the planar state (off state), the focal conic state (40 V at 500 Hz), and the homeotropic state (200 V at 500 Hz), respectively, in the reflection mode under two crossed polarizers. Scale bar: 500 μm.

state, they become a light shutter since the LC molecules form a multi-domain structure, resulting in an opaque appearance due to strong scattering; and in the homeotropic state, all the LC molecules will be aligned perpendicular to the substrate, and the DF-CLCs become totally transparent, as a result, they do not change the polarization state of the incident light.[55–57]

As is known,[58] the helical pitch p of CLCs can be calculated with

$$p = \frac{1}{c \times \mathrm{HTP}}, \tag{4}$$

where c is the concentration of the chiral dopant and HTP is the helical twisting power of the chiral dopant. Due to the periodic helical structure in CLCs, strong Bragg reflection occurs. Within the Bragg reflection band, depending on the handedness of CLCs, the unpolarized or linearly polarized incident light will be converted to circularly polarized light with the same handedness in reflection mode and the opposite handedness in transmission mode. The centre wavelength λ of the Bragg reflection band of DF-CLCs can be calculated with

$$\lambda = p \times \frac{n_o + n_e}{2}, \tag{5}$$

where n_o and n_e are the ordinary and extraordinary refractive indices, respectively. The Bragg reflection bandwidth $\Delta\lambda$ can be written as

$$\Delta\lambda = \Delta n p, \tag{6}$$

where $\Delta n = n_e - n_o$.

In our experiment, DF-CLCs are a mixture of the right-handed chiral dopant, R5011, and the DFLCs, DP02-016. The alignment of DFLCs can be switched between homogeneous and homeotropic states by applying an electric field with a low or high frequency. The HTP of the chiral dopant R5011 is 94 μm^{-1}. With the centre wavelength λ of the Bragg reflection band designed to be 633 nm, the pitch of CLCs and the concentration of the chiral dopant R5011 are calculated to be 385 nm and 2.9 wt%, respectively. Within the bandgap regime, under the normal incidence, highly acceptable circular polarization of the transmitted light can be achieved when the CLC thickness is larger than 10 pitches[46–49] (see Fig. S5†). In our experiment, the DF-CLC cell gap was controlled to be 20 μm (about ~53 pitches) using a ball spacer. With such a DF-CLC mixture, we have investigated its textures under a polarizing optical microscope. Fig. 3(d)–(f) respectively show the planar, focal conic, and homeotropic states of DF-CLCs under two crossed polarizers. The planar state demonstrates the Bragg reflection in the red range. Upon applying an AC voltage of 40 V with a low frequency of 500 Hz, the planar state is changed to the focal conic state, hence inducing strong scattering of incident light and resulting in an opaque appearance. When further increasing the voltage to 200 V with the same frequency, all the LC molecules are realigned along the electric field direction, producing a totally transparent state. When a low AC voltage of 40 V was applied with a high frequency of 200 kHz, the focal conic state of DF-CLCs transforms entirely into the planar state. While when a high AC voltage of 200 V was applied with a high frequency of 200 kHz, the homeotropic state of DF-CLCs reverts to the planar state. In addition, we measured the switching speed among the inter-transformable states. The switching times are 790, 1150, and 580 ms when the DF-CLCs change from the planar state to the focal conic state by applying the AC voltage of 40 V with the low frequency of 500 Hz, from the focal conic state to the homeotropic state by applying an AC voltage of 200 V with a low frequency of 500 Hz, and from the focal conic state to the planar state by applying an AC voltage of 40 V with a high frequency of 200 kHz.

As a polarization controller, the performance of the DF-CLC cell was further tested. First, the transmission was measured for the laser beam with the working wavelength of 633 nm (within the Bragg reflection band) by applying different voltages with a low frequency of 500 Hz and a high frequency of 200 kHz, respectively, as shown in Fig. 4(a). We can see that at the low driving frequency, the transmission of the DF-CLC cell undergoes a drastic change in different texture states when applying different voltages. Experimental results show that the DF-CLC cell has the transmission of 60% in the planar state, 35% in the focal conic state, and 80% in the homeotropic state, respectively. While at the high driving frequency, it has a

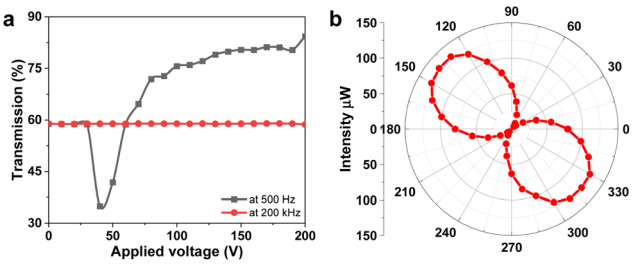

Fig. 4 (a) Voltage-dependent electro-optic transmission of the DF-CLC cell at 500 Hz and 200 kHz, respectively. (b) Polar plot of the polarization-dependent intensity of the transmitted light through the DF-CLC cell.

nearly constant transmission of 60%, which is independent of the applied voltage. The broadband transmission of the DF-CLC cell in the whole visible range was also measured under the unpolarized light incidence, as shown in Fig. S6.† To give an intuitive sense of the transmittance of the DF-CLC cell, Fig. S7† shows photographs taken in the planar, focal conic, and homeotropic states with natural light. Furthermore, we used a home-made setup as shown in Fig. S8(a)† to characterize the circular polarization properties of the transmitted light when light passes through the DF-CLC cell. Assuming that the light transmitted through the DF-CLCs has a polarization angle θ with respect to the fast axis of the quarter-wave plate, the Jones matrix of the quarter-wave plate can be written as:

$$J_{\lambda/4} = \begin{bmatrix} \cos^2\theta + i\sin^2\theta & \cos\theta\sin\theta(1-i) \\ \cos\theta\sin\theta(1-i) & i\cos^2\theta + \sin^2\theta \end{bmatrix}, \quad (7)$$

when the incident light is left (or right) circularly polarized light $E_{in} = [1, -i]^T$, or $[1, i]^T$ through a quarter-wave plate, the transmitted light E_{out} can be written as:

$$E_{out} = \begin{bmatrix} \cos^2\theta + i\sin^2\theta & \cos\theta\sin\theta(1-i) \\ \cos\theta\sin\theta(1-i) & i\cos^2\theta + \sin^2\theta \end{bmatrix} \begin{bmatrix} 1 \\ \pm i \end{bmatrix}$$
$$= \begin{cases} (\cos\theta + i\sin\theta)(\cos\theta + \sin\theta)\begin{bmatrix} 1 \\ \tan(\theta - \frac{\pi}{4}) \end{bmatrix}, & \text{when } E_{in} = \begin{bmatrix} 1 \\ i \end{bmatrix} \\ (\cos\theta - i\sin\theta)(\cos\theta - \sin\theta)\begin{bmatrix} 1 \\ \tan(\theta + \frac{\pi}{4}) \end{bmatrix}, & \text{when } E_{in} = \begin{bmatrix} 1 \\ -i \end{bmatrix} \end{cases}. \quad (8)$$

From eqn (8), if the fast axis of the quarter-wave plate and the optical axis of the circularly polarized light are placed at any angle, the circularly polarized light can be converted into linearly polarized light. Therefore, we can evaluate the degree of polarization of the linearly polarized light by putting another linear polarizer behind the quarter-wave plate. Fig. S8(b)† shows the measured light intensity as a function of the rotation angle of the linear polarizer. The achieved degree of polarization is larger than 0.93, indicating that the light is almost circularly polarized when passing through the DF-CLC cell. Fig. 4(b) shows the polar plot of the light intensity with the rotation angle of the polarizer. Since the dopant R5011 is a right-handed chiral molecule, the filtered light by DF-CLCs is then LCP. We have made a summary of the achieved polarizations when different polarized light beams pass through the QWP, as shown in Table S1.†

2.3 DF-CLC-enabled electrically programmable metasurfaces

With the understanding of the characteristics of both designed metasurfaces and DF-CLCs, it is straightforward to integrate them together to achieve electrically programmable functions. Fig. 5 shows the schematic design of the electrically programmable metasurface enabled by DF-CLCs. The integrated device can be inter-transformed among the three states by applying frequency-modulated voltage pulses. Fig. 6(a)–(c) experimentally demonstrate the far-field displays (*i.e.*, diffracted images in the *k*-space of the designed hologram) in the three states of DF-CLCs. Meanwhile, Fig. 6(d)–(f) illustrate the near-field displays (*i.e.*, structural coloration-induced images in real space) in the three corresponding states. It is worth mentioning that the far-field displays can only be achieved for monochromatic light (633 nm in this work), while the near-field displays work for broadband visible light. As a result, the integrated device can produce a high-quality diffracted image of "photonics" and a structural color image of "NANO" in the planar state, as shown in Fig. 6(a) and (d).

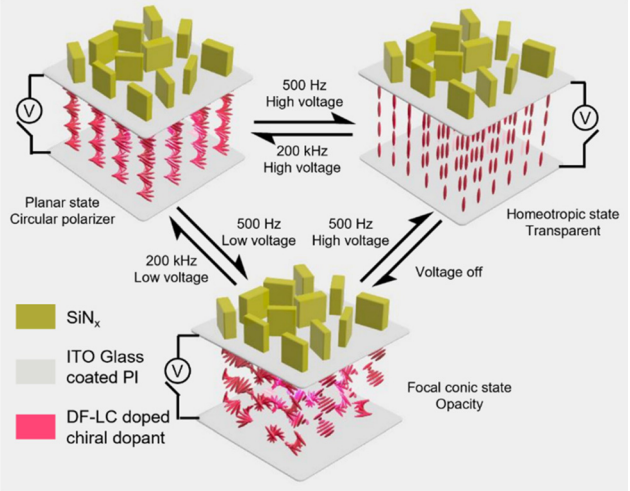

Fig. 5 Schematic diagram of a DF-CLC-enabled electrically programmable metasurface.

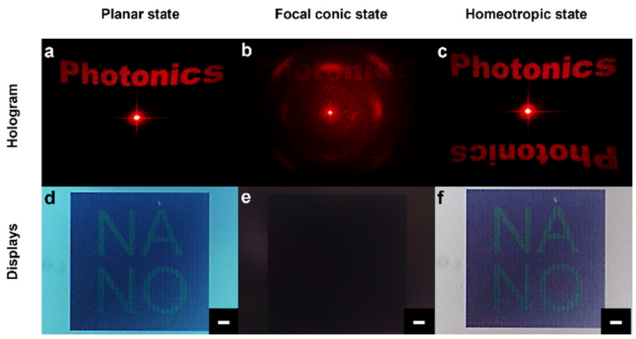

Fig. 6 Experimental demonstration of the electrically programmable metasurface enabled by DF-CLCs. (a–c) The far-field display (*i.e.*, hologram) under the linearly polarized 633 nm laser beam incidence and (d–f) the near-field display (*i.e.*, structural color) under unpolarized light incidence in the planar, focal conic, and homeotropic states, respectively. Scale bar: 50 μm.

Upon applying an AC voltage of 40 V with a low frequency of 500 Hz, the DF-CLCs transform to the focal conic state, resulting in a strong scattering state. Therefore, both far- and near-field displays can be blocked, as shown in Fig. 6(b) and (e). When further increasing the voltage to 200 V with the same frequency, all the LC molecules are realigned along the electric field direction, producing a totally transparent state. In

this state, the near-field display reappears. While the incident laser light to the metasurface becomes linearly polarized, hence resulting in a conjugated image. Finally, the DF-CLCs can return to a planar state after applying a high voltage with a high frequency (200 V at 200 kHz). Therefore, the integrated device can be electrically programmed to demonstrate 6 different optical images by engineering the DF-CLCs with frequency-modulated voltage pulses.

Per the above discussion, we generated six different images *via* electrically programming the DF-CLCs' states by changing the driving voltage and frequency. However, it is undeniable that there is information overlapping presented in Fig. 6. However, much more information can be further encoded using different multiplexing techniques.[59,60] Furthermore, although the DF-CLCs are prone to the dielectric heating effect and frequency drift due to dielectric anisotropy changes,[61] this generally occurs when a high voltage is applied for a long time. With deliberate control and material optimization, this detrimental effect could be largely avoided.

3. Conclusions

In summary, we have demonstrated an electrically programmable metasurface enabled by DF-CLCs for simultaneous near- and far-field displays. The DF-CLCs can be programmed to demonstrate the planar, focal conic and homeotropic states, respectively, hence indicating that the light passing through them have different polarizations. Based on these characteristics of DF-CLCs, the integrated metasurface with DF-CLCs can be electrically programmed to demonstrate 6 different optical images by engineering the DF-CLCs with frequency-modulated voltage pulses. Such a device eliminates the bulky optical setup for the polarization conversion of the incident light and presents highly integrated, compact, and programmable features. More importantly, such a device can achieve both near- and far-field multiplexed displays, hence increasing the information capacity significantly. Such programmable metasurfaces are potentially useful for many applications including information storage, displays, anti-counterfeiting, and so on.

4. Methods

4.1 Nanofabrication

The designed metasurfaces were fabricated on the nonconductive side of an indium–tin-oxide (ITO)-coated glass substrate. The ITO-coated glass substrate was ultrasonically cleaned with acetone and isopropyl alcohol (IPA). Following that, a 900 nm-thick SiN_x film was deposited on the nonconductive side of the ITO-coated glass substrate using plasma-enhanced chemical vapor deposition (PECVD, PlasmaPro 80, Oxford). The deposition conditions were 350 °C substrate temperature, 1400 mTorr pressure, $SiH_4/NH_3/N_2$ = 6.5/4.0/823.5 sccm gas flow and mixing of high (25 W RF) and low (35 W LF) frequency power. Then a positive electron beam resist (AR-P 6200.09) was spin-coated on the SiN_x thin film. The resist layer was about 150 nm thick, followed by prebaking at 150 °C for 2 min. Subsequently, a thin layer of conductive solution (AR-PC 5090.02) was further spin-coated to prevent the charge accumulation effect during subsequent electron beam exposure. After that, electron-beam lithography (EBL, nB5, Nano beam) was carried out with 230 μC cm^{-2} at the 2 nA current and 80 kV voltage. The development of an exposed substrate was done in a solution of AR 600-546 for 60 s. After development, a 50 nm chromium layer was deposited on the resist pattern using an electron beam evaporation system (TF-500, HHV). The evaporation rate was controlled to be ≈0.08 Å s^{-1} with the vacuum level of 5 × 10^{-6} Torr inside the evaporator chamber. A Cr hard mask was achieved successfully after a lift-off process in the resist remover (AR 600-71). To pattern the SiN_x thin film, inductively coupled plasma-reactive ion etching (ICP-RIE, GSE200Plus, North Microelectronics Company) treatment was implemented for 1100 s with CHF_3/O_2/Ar mixed gases. Finally, the metasurfaces were achieved after the Cr hard mask was removed in a chromium etchant solution (1020, Transene).

4.2 DF-CLC cell fabrication

DF-CLCs consisting of 2.9 wt% chiral dopant R5011 (Jiangsu Hecheng Display Co., Ltd) and 98.1 wt% DFLCs DP002-016 (Jiangsu Hecheng Display Co., Ltd) were stirred at 120 °C for 1 hour to achieve a homogeneous solution. The ordinary and extraordinary refractive indices of DP002-016 are n_o = 1.511 and n_e = 1.784 at 546 nm at room temperature, respectively. To make a cell, a polyimide (PI, DL-5260, DALTON) solution was spin-coated on the ITO side of metasurfaces, and another cleaned ITO-coated glass substrate and then baked in an oven at 200 °C for 2 h. The measured thickness of the PI layer was 100 nm. Subsequently, the PI layers were rubbed using a rubbing machine (LHC-MC-V1, HCPE). Two pieces of the ITO-coated glass substrates, with the rubbed PI alignment layers, were then assembled to form a parallel LC cell with the optical adhesive NOA65. The cell gap was controlled to be 20 μm using the ball spacer. An appropriate thickness of DF-CLC cells can not only ensure excellent Bragg reflection performance but also a reasonable driving voltage and response time. Finally, the DF-CLCs were injected into the cell through capillary action at an isotropic temperature of 120 °C and then slowly cooled down to room temperature.

4.3 Numerical simulation

The refractive index of the SiN_x thin film was obtained using ellipsometry (Horiba, UVISEL) in the spectral range of 400–800 nm. The optical intensity and PB phase of the metasurfaces were calculated using the finite-difference time-domain (FDTD) method. A unit cell of the PB-phase based metasurface was simulated with periodic boundary conditions (*x*- and *y*-directions) and a perfectly matched layer (PML) (*z*-direction). A plane wave ranging from 400 to 800 nm with circular polarization was normally incident from the bottom,

reaching the glass substrate first. Auto-uniform meshing with the finest-mesh of 2 nm was used to achieve accurate results. Two power monitors were separately located ±1.5 μm above the metasurface to collect the transmitted/reflected optical intensity and phase, respectively. A series of simulations were carried out for different sets of width-to-length ratios and heights of meta-atoms to achieve the best conversation efficiency and high intensity.

4.4 Characterization

The surface morphologies of silicon nitride metasurfaces were investigated under a field-emission scanning electron microscope (FESEM, GeminiSEM 300-71-10, Zeiss) with an acceleration voltage of 3 kV. The optical spectra of the samples were recorded using a UV–vis–NIR microspectrophotometer (CRAIC Technologies Inc.) with a 75 W broadband xenon source. An optical microscope (Nikon Eclipse, Ci POL) was used to check the DF-CLC textures and observe the near-field displays. A CCD camera (Nikon DS-Fi2) mounted on the microscope was used for optical image acquisition. We characterized the properties of DF-CLCs and metasurface holograms with a 633 nm He–Ne laser (Research Electro-Optics Inc.). The DF-CLCs were driven by a square-wave voltage with a frequency of 500 Hz or 200 kHz from a signal generator (ATA-2041, Aigtek, China).

Conflicts of interest

There are no conflicts to declare.

Acknowledgements

This work was supported in part by the National Key R&D Program of China (grant no. 2021YFB2802300), the National Natural Science Foundation of China (grant no. 62075093 and 62211530039), the Guangdong Innovative and Entrepreneurial Research Team Program (grant no. 2017ZT07C071), the Natural Science Foundation of Guangdong Province (grant no. 2019A1515110864), and the Shenzhen Science and Technology Innovation Commission (grant no. JCYJ20180305180635082, JCYJ20170817111349280, and GJHZ20180928155207206). This study was also funded by the Key Lab of Modern Optical Technologies of Education Ministry of China, Soochow University (grant no. KJS2132). The authors acknowledge the assistance of SUSTech Core Research Facilities.

References

1 N. Yu, P. Genevet, M. A. Kats, F. Aieta, J. P. Tetienne, F. Capasso and Z. Gaburro, *Science*, 2011, **334**, 333.
2 G. Zheng, H. Mühlenbernd, M. Kenney, G. Li, T. Zentgraf and S. Zhang, *Nat. Nanotechnol.*, 2015, **10**, 308.
3 L. Dianmin, F. Pengyu, H. Erez and M. L. Brongersma, *Science*, 2016, **345**, 298.
4 A. Arbabi, Y. Horie, M. Bagheri and A. Faraon, *Nat. Nanotechnol.*, 2015, **10**, 937.
5 N. Yu, F. Aieta, P. Genevet, M. A. Kats, Z. Gaburro and F. Capasso, *Nano Lett.*, 2012, **12**, 6328.
6 W. T. Chen, K. Y. Yang, C. M. Wang, Y. W. Huang, G. Sun, I. Da Chiang, C. Y. Liao, W. L. Hsu, H. T. Lin, S. Sun, L. Zhou, A. Q. Liu and D. P. Tsai, *Nano Lett.*, 2014, **14**, 225.
7 R. C. Devlin, A. Ambrosio, N. A. Rubin, J. P. B. Mueller and F. Capasso, *Science*, 2017, **358**, 896.
8 A. C. Overvig, S. Shrestha, S. C. Malek, M. Lu, A. Stein, C. Zheng and N. Yu, *Light: Sci. Appl.*, 2019, **8**, 1.
9 Z. Deng, M. Jin, X. Ye, S. Wang, T. Shi, J. Deng, N. Mao, Y. Cao, B. Guan, A. Alù, G. Li and X. Li, *Adv. Funct. Mater.*, 2020, **30**, 1910610.
10 J. Zhang, X. Wei, I. D. Rukhlenko, H. T. Chen and W. Zhu, *ACS Photonics*, 2020, **7**, 265.
11 W. Yang, S. Xiao, Q. Song, Y. Liu, Y. Wu, S. Wang, J. Yu, J. Han and D.-P. Tsai, *Nat. Commun.*, 2020, **11**, 1864.
12 S. Colburn, A. Zhan and A. Majumdar, *Sci. Adv.*, 2018, **4**, eaar2114.
13 W.-J. Joo, J. Kyoung, M. Esfandyarpour, S.-H. Lee, H. Koo, S. Song, Y.-N. Kwon, S. H. Song, J. C. Bae, A. Jo, M.-J. Kwon, S. H. Han, S.-H. Kim, S. Hwang and M. L. Brongersma, *Science*, 2020, **370**, 459.
14 W. T. Chen, A. Y. Zhu and F. Capasso, *Nat. Rev. Mater.*, 2020, **5**, 604.
15 M. K. Chen, Y. Wu, L. Feng, Q. Fan, M. Lu, T. Xu and D. P. Tsai, *Adv. Opt. Mater.*, 2021, **9**, 2001414.
16 X. Ni, A. V. Kildishev and V. M. Shalaev, *Nat. Commun.*, 2013, **4**, 2807.
17 S. Chen, W. Liu, Z. Li, H. Cheng and J. Tian, *Adv. Mater.*, 2020, **32**, 1805912.
18 J. Chen, C. Wan and Q. Zhan, *Sci. Bull.*, 2018, **63**, 54.
19 C. Jung, G. Kim, M. Jeong, J. Jang, Z. Dong, T. Badloe, J. K. W. Yang and J. Rho, *Chem. Rev.*, 2021, **121**, 13013.
20 R. Zhao, B. Sain, Q. Wei, C. Tang, X. Li, T. Weiss, L. Huang, Y. Wang and T. Zentgraf, *Light: Sci. Appl.*, 2018, **7**, 95.
21 M. Khorasaninejad, A. Ambrosio, P. Kanhaiya and F. Capasso, *Sci. Adv.*, 2016, **2**, e1501258.
22 Z. L. Deng, J. Deng, X. Zhuang, S. Wang, K. Li, Y. Wang, Y. Chi, X. Ye, J. Xu, G. P. Wang, R. Zhao, X. Wang, Y. Cao, X. Cheng, G. Li and X. Li, *Nano Lett.*, 2018, **18**, 2885.
23 P. Georgi, Q. Wei, B. Sain, C. Schlickriede, Y. Wang, L. Huang and T. Zentgraf, *Sci. Adv.*, 2021, **7**, eabf9718.
24 Y. Hu, X. Luo, Y. Chen, Q. Liu, X. Li, Y. Wang, N. Liu and H. Duan, *Light: Sci. Appl.*, 2019, **8**, 86.
25 J. Kim, D. Jeon, J. Seong, T. Badloe, N. Jeon, G. Kim, J. Kim, S. Baek, J.-L. Lee and J. Rho, *ACS Nano*, 2022, **16**, 3546.
26 Y. Bao, Y. Yu, H. Xu, C. Guo, J. Li, S. Sun, Z.-K. Zhou, C.-W. Qiu and X.-H. Wang, *Light: Sci. Appl.*, 2019, **8**, 95.
27 Q. Dai, Z. Guan, S. Chang, L. Deng, J. Tao, Z. Li, Z. Li, S. Yu, G. Zheng and S. Zhang, *Adv. Funct. Mater.*, 2020, **30**, 2003990.
28 Y. J. Liu, Q. Z. Hao, J. S. T. Smalley, J. Liou, I. C. Khoo and T. J. Huang, *Appl. Phys. Lett.*, 2010, **97**, 091101.

29 Y. J. Liu, E. S. P. Leong, B. Wang and J. H. Teng, *Plasmonics*, 2011, **6**, 659.
30 Y. J. Liu, X. Y. Ding, S.-C. S. Lin, J. J. Shi, I.-K. Chiang and T. J. Huang, *Adv. Mater.*, 2011, **23**, 1656.
31 Y. J. Liu, G. Y. Si, E. S. P. Leong, N. Xiang, A. J. Danner and J. H. Teng, *Adv. Mater.*, 2012, **24**, OP131.
32 K. Chen, C. Xu, Z. Zhou, Z. Li, P. Chen, G. Zheng, W. Hu and Y. Lu, *Laser Photonics Rev.*, 2022, **16**, 2100591.
33 I. Kim, J. Jang, G. Kim, J. Lee, T. Badloe, J. Mun and J. Rho, *Nat. Commun.*, 2021, **12**, 3614.
34 C. Wan, Z. Li, S. Wan, C. Dai, J. Tang, Y. Shi and Z. Li, *Adv. Funct. Mater.*, 2022, **32**, 2110592.
35 I. Kim, W. S. Kim, K. Kim, M. A. Ansari, M. Q. Mehmood, T. Badloe, Y. Kim, J. Gwak, H. Lee, Y. K. Kim and J. Rho, *Sci. Adv.*, 2021, **7**, eabe9943.
36 M. Bosch, M. R. Shcherbakov, K. Won, H. S. Lee, Y. Kim and G. Shvets, *Nano Lett.*, 2021, **21**, 3849.
37 I. Kim, M. A. Ansari, M. Q. Mehmood, W. Kim, J. Jang, M. Zubair, Y. Kim and J. Rho, *Adv. Mater.*, 2020, **32**, 2004664.
38 Y. Hu, X. Ou, T. Zeng, J. Lai, J. Zhang, X. Li, X. Luo, L. Li, F. Fan and H. Duan, *Nano Lett.*, 2021, **21**, 4554.
39 J. Li, S. Kamin, G. Zheng, F. Neubrech, S. Zhang and N. Liu, *Sci. Adv.*, 2018, **4**, eaar6768.
40 K. Li, J. Wang, W. Cai, H. He, M. Cen, J. Liu, D. Luo, Q. Mu, D. Gérard and Y. J. Liu, *Nano Lett.*, 2021, **21**, 7183.
41 K. Li, J. Wang, W. Cai, H. He, J. Liu, Z. Yin, D. Luo, Q. Mu, D. Gérard and Y. J. Liu, *Opt. Express*, 2022, **30**, 31913.
42 J. Wang, K. Li, H. He, W. Cai, J. Liu, Z. Yin, Q. Mu, V. K. S. Hisao, D. Gérard, D. Luo, G. Li and Y. J. Liu, *Laser Photonics Rev.*, 2022, **16**, 2100396.
43 G. Y. Si, Y. H. Zhao, E. S. P. Leong and Y. J. Liu, *Materials*, 2014, **7**, 1296.
44 D. Wang, C. Liu, C. Shen, Y. Xing and Q.-H. Wang, *PhotoniX*, 2020, **1**, 6.
45 Y.-L. Li, N.-N. Li, D. Wang, F. Chu, S.-D. Lee, Y.-W. Zheng and Q.-H. Wang, *Light: Sci. Appl.*, 2022, **11**, 188.
46 D. Grzelczyk and J. Awrejcewicz, *Reflectance and transmittance of cholesteric liquid crystal sandwiched between polarizers*, Springer, Cham, Switzerland, 2018.
47 R. H. Good and A. Karali, *J. Opt. Soc. Am. A*, 1994, **11**, 2145.
48 D. K. Yang and X. D. Mi, *J. Phys. D: Appl. Phys.*, 2000, **33**, 672.
49 P. V. Dolganov, K. D. Baklanova and V. K. Dolganov, *J. Exp. Theor. Phys.*, 2020, **130**, 790.
50 P. Chen, L.-L. Ma, W. Duan, J. Chen, S.-J. Ge, Z.-H. Zhu, M.-J. Tang, R. Xu, W. Gao, T. Li, W. Hu and Y.-Q. Lu, *Adv. Mater.*, 2018, **30**, 1705865.
51 P. Chen, L.-L. Ma, W. Hu, Z.-X. Shen, H. K. Bisoyi, S.-B. Wu, S.-J. Ge, Q. Li and Y.-Q. Lu, *Nat. Commun.*, 2019, **10**, 2518.
52 P. Chen, B. Wei, W. Hu and Y. Lu, *Adv. Mater.*, 2019, **32**, 1903665.
53 P. Chen, Z. Shen, C. Xu, Y. Zhang, S. Ge, L. Ma, W. Hu and Y. Lu, *Laser Photonics Rev.*, 2022, **16**, 2200011.
54 L. Zhu, C.-T. Xu, P. Chen, Y.-H. Zhang, S.-J. Liu, Q.-M. Chen, S.-J. Ge, W. Hu and Y.-Q. Lu, *Light: Sci. Appl.*, 2022, **11**, 135.
55 C. S. Lee, T. A. Kumar, J. H. Kim, J. H. Lee, J. S. Gwag, G.-D. Lee and S. H. Lee, *J. Mater. Chem. C*, 2018, **6**, 4243.
56 P. Kumar, S.-W. Kang and S. H. Lee, *Opt. Mater. Express*, 2012, **2**, 1121.
57 X. Du, Y. Li, Y. Liu, F. Wang and D. Luo, *Liq. Cryst.*, 2019, **46**, 1727.
58 P. G. De Gennes and J. Prost, *The Physics of Liquid Crystal*, Oxford University Press, Oxford, UK, 2nd edn, 1993.
59 K. Huang, Z. Dong, S. Mei, L. Zhang, Y. Liu, H. Liu, H. Zhu, J. Teng, B. Luk'yanchuk, J. K. W. Yang and C.-W. Qiu, *Laser Photonics Rev.*, 2016, **10**, 500.
60 W. Wan, W. Yang, H. Feng, Y. Liu, Q. Gong, S. Xiao and Y. Li, *Adv. Opt. Mater.*, 2021, **9**, 2100626.
61 C.-H. Wen and S.-T. Wu, *Appl. Phys. Lett.*, 2005, **86**, 231104.